ACS OMEGA

Article

Cite This: ACS Omega 2018, 3, 4433−4440

Development of Low-ppm CO Sensors Using Pristine CeO_2 Nanospheres with High Surface Area

Deblina Majumder and Somenath Roy*

Sensor and Actuator Division, CSIR-Central Glass and Ceramic Research Institute, 196 Raja S.C. Mullick Road, Kolkata 700032, India

Supporting Information

ABSTRACT: Mesoporous CeO_2 nanospheres with appreciably high surface area are prepared using reversed micelles by a water-in-oil microemulsion method. The structural morphology and semiconducting properties of the nanoparticles are thoroughly investigated using X-ray diffraction, field effect scanning electron microscopy, transmission electron microscopy, and UV−visible spectroscopic techniques. Even after high-temperature calcination, the morphological retention of the material is apparent by electron microscopy. The deployment of undoped CeO_2 nanospheres for the detection of low-ppm CO yields superior performances in terms of sensitivity, response−recovery times, and selectivity compared to those of other sensors of the same genre. These CO sensors exhibit ∼ 52% sensitivity with a response time of only 13 s. The sensor parameters are analyzed as a function of both temperature and gas concentration. In addition to that on the cost-effective and scalable synthesis of CeO_2 nanospheres, this article also reports on the fabrication of packaged CO sensors, which can be potentially utilized for industrial and environmental monitoring purposes.

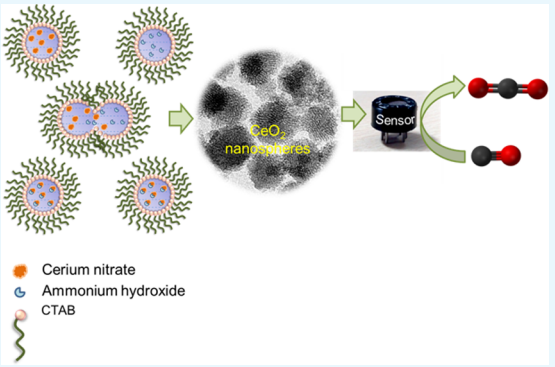

INTRODUCTION

CeO_2 is a widely applied rare-earth oxide material in many fields such as catalysts, optics, and gas sensors because of its unique properties, arising peculiarly from its 4f shells.[1] Cerium being the most abundant nontoxic element in the Earth's crust, CeO_2 is one of the most used catalysts for the reduction of toxic gases, like CO, NO_x, hydrocarbons, etc., emit from automobile exhausts. High oxygen storage capacity, huge oxygen vacancies, and low redox potential between Ce^{3+} and Ce^{4+} have made this oxide an advantageous sensing material toward reducing gases.[2−6] Because of the rapid growth of industries and population, CO is one of the most life-threatening gases in today's world causing severe health hazards. As per the specifications of World Health Organization (WHO) and Occupational Safety and Health Administration (OSHA), the time-weighted average exposure limit of carbon monoxide is 9 ppm for 8 h, 26 ppm over 1 h, and 35 ppm for 8 h, respectively. Thus it is essential to develop sensors for the detection of CO in air below the permissible exposure limit with fast alarming response.[7,8] Although CeO_2 is reported to be one of the most suitable materials for the said purpose because of its aforementioned advantageous properties, very few reports are available in the literature on the development of CO sensors using undoped bare pristine CeO_2. There are reports on the detection of oxygen by resistive CeO_2 sensors, consisting of thick or thin films of CeO_2.[9,10] The morphological properties and surface porosities have also been analyzed in the light of their sensing performances.[11−13] Xuan et al. reported the development of a CS_2−CeO_2 sensor where the intensity of the emitted chemiluminescence was recorded as a signal, associated with the gas concentration.[14] Izu et al. furnished a screen-printed thick film CeO_2 sensor for SO_2 gas sensing application.[15] More such articles are published on CO sensing using doped, undoped, or composites of ceria.[16,17] Durrani et. al reported on the CO gas-sensing properties of electron-beam-deposited CeO_2 thin films where the lower limit of detection (LOD) was 500 ppm at the operating temperature of 390 °C having response and recovery times of 45 and 25 s, respectively.[18] Michel and his co-workers have synthesized a three-dimensional hierarchical CeO_2 nanostructure following a simple microwave-assisted coprecipitation method and deployed the same for CO sensing. Although the operating temperature of their bare CeO_2-based CO sensors was lowered with fast response and recovery times, the LOD of the sensors was 300 ppm, which is impractically high for real-field application.[19]

This work outlines the reverse micelle method for synthesizing highly porous CeO_2 nanomaterials with the plausible formation mechanism and deployment of bare materials for low-ppm CO gas sensing application. The influence of the porosity of the material is discussed as morphological boon toward CO sensing. We also report on the optimum operating

Received: January 24, 2018
Accepted: March 28, 2018
Published: April 24, 2018

DOI: 10.1021/acsomega.8b00146
ACS Omega 2018, 3, 4433−4440

temperature and appreciably fast response−recovery times of the sensors for real-field application purposes, which are comparably better than those of any other sensors of the same genre. The longibility of the said sensors is also studied in terms of their respective sensor parameters.

EXPERIMENTAL SECTION

Material Synthesis. All of the chemicals of analytical grade were purchased from Sigma-Aldrich and used without further purifications. First, a microemulsion was prepared by mixing diethyl ether, *n*-butyl alcohol, and *n*-hexane in the weight ratio 1:2:3 with vigorous stirring until the mixture became transparent. The amount of cetyl trimethylammonium bromide (CTAB) to form critical micelle concentration (CMC) was determined following the standard conductometric method, where a series of microemulsions were analyzed varying the CTAB concentration from 0.2 to 1.5 g (detailed in Figure S1). Then, 10 mL of 1 M aqueous solution of cerium nitrate containing 0.65 g of CTAB was added to the mixture and the mixture was stirred again till it became transparent. Simultaneously, another aqueous solution of 10% (w/v) NH_4OH was prepared. The above solutions were mixed vigorously until a colloidal suspension was formed. The material was collected by centrifugation at 6000 rpm for 30 min and successively washed using deionized water in an ultrasonic bath for 2 h. Finally, the collected material was dried under vacuum and calcined at 600 °C for 4 h.

Characterization Techniques. The phase analysis of the sample was carried out using an X-ray diffractometer (Bruker D8 Advance, Cu Kα line). Morphological analyses were performed by a field effect scanning electron microscope (FESEM CarlZeiss-Supra35VP) system and high resolution transmission electron microscope (HRTEM, model: TECNAI G2 30ST; manufacturer: FEI Company, The Netherlands). The optical property was studied using Shimadzu UV 2450, and the Brunauer−Emmett−Teller (BET) surface area was measured using Quantachrome Instruments, version 3.0. Dynamic light scattering (DLS) measurements were performed using a Nano S Malvern instrument deploying a 4 mW He−Ne laser (I 1/ 4632.8 nm), which is equipped with a thermostated sample chamber. The scattered photons are collected at a scattering angle of 173°. Photoluminescence (PL) spectroscopy was performed using a Horiba Jobin Yvon Fluorolog fluorimeter by irradiating the sample at λ_{ex} = 320 nm. During CMC determination, the conductometric measurement was carried out using an HI 8733 conductivity meter.

Fabrication of Sensors. Gas-sensing measurements were performed using Taguchi-type sensors consisting of an insulating cylindrical alumina substrate with terminal gold electrodes (using gold paste and cured at 950 °C for 1 h).[17] During substrate making, the alumina tubes were cut into specific dimensions (length 4 mm, outer diameter 2 mm, and inner diameter 1 mm). After that, both the edges of the tubes were polished vigorously using sand paper and washed using HCl, distilled water, and finally acetone. Connecting wires of Platinum were attached to these tubular substrates and mounted onto a 6-pin holder by spot-welding. The sensor substrate had a coaxial heating element inside (Ni−Cr wire), and the sensing CeO_2 material was coated on top of it using isopropyl alcohol. The viscosity of the coating material was optimized to get a final coating of around 50 μm thickness. The curing of sensors was done at 400 °C for 1 h. The curing process brings stability to the coating. Finally, the sensors were packaged by spot-welding on nickel pins fixed on polymer sensor heads and covered with a stainless steel mesh. The mesh works as a deflagration arrester.

Gas-Sensing Measurement. Upon injection of a target analyte (CO in air in the concentration range of 10−30 ppm), the drop in resistance of the sensors was measured as a signal by an Agilent B2901A Source Meter using LabView-based graphical user interface. A series of mass flow controllers were used to get the desired CO concentration at 1 atm pressure under the flow rate of 50 sccm. It is to be mentioned that the required operating temperature for the sensor module was set by changing the current driven through the heating element (Ni−Cr wire), which was inserted in the alumina substrate.

RESULTS AND DISCUSSION

Crystallographic and Morphological Analyses. Crystallographic analysis of the synthesized material reveals the formation of anatase CeO_2 nanostructures, and the peaks at (111), (200), (220), (311), (222), (400), and (331) in Figure 1

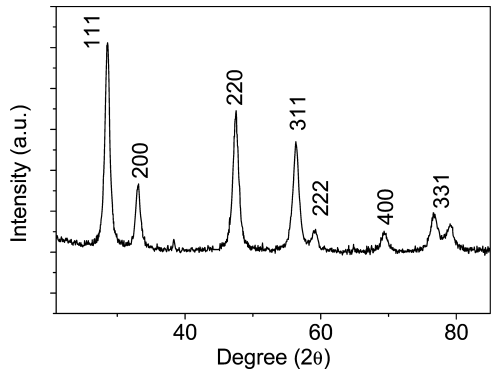

Figure 1. X-ray diffraction pattern of CeO_2 nanoparticles showing characteristic crystallographic peaks of the fcc phase.

match with the face-centered cubic (fcc) phases as provided in JCPDS card no. 34-1394. Figure 2 shows the morphology of the CeO_2 materials. Figure 2a,b is the FESEM and TEM micrographs, respectively. They show the formation of spherelike structures. The well-dispersed nanospheres are of average diameter ∼50 nm. The inset of Figure 2a depicts the particle size distribution plot showing the average diameter of the particles to be 50−55 nm. The inset of Figure 2b presents the HRTEM image of the nanospheres showing the characteristic lattice fringes of CeO_2. Another FESEM image of monodispersed spherical CeO_2 nanoparticles is provided in Figure S2. Figure 2c provides the energy dispersive X-ray analysis (EDAX) analyses of the material, showing the peak of only Ce, which confirms that no other impurity is present. Figure 2d represents the selected area electron diffraction (SAED) pattern showing bright spots referring to crystalline nature of the sample. The retention of spherical morphology of CeO_2 is found to be unaltered after calcination at 600 °C. The corresponding TEM micrograph is provided in the Supporting Information Section (Figure S3). The nitrogen adsorption−desorption isotherm study was carried out, and the determined Brunauer−Emmett−Teller (BET) specific surface area of the CeO_2 materials was found to be 773.31 cm^3/g, which is moderately high. Figure 3 delineates the corresponding isotherm with the pore size distribution curve (inset). As expected, because of the high surface area, the CeO_2 nanospheres are found to be porous in nature with average

DOI: 10.1021/acsomega.8b00146
ACS Omega 2018, 3, 4433−4440

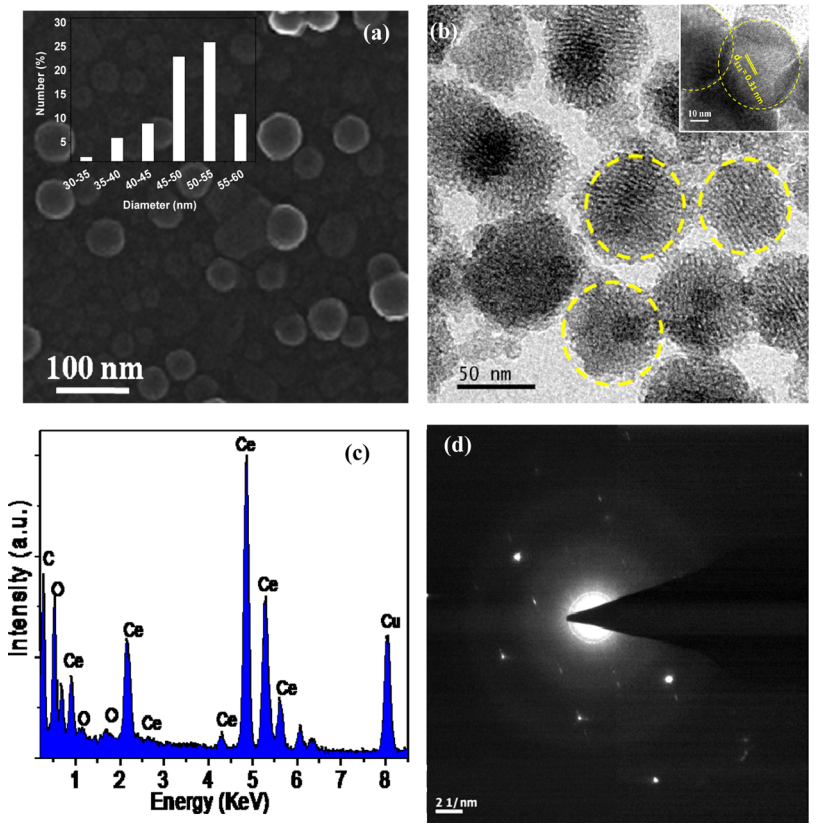

Figure 2. (a) FESEM micrograph of CeO_2 nanospheres, and particle size distribution is provided in the inset, (b) TEM image of well-dispersed nanoparticles with the HRTEM image (inset) showing the characteristic *d*-spacing of ceria, (c) and (d) corresponding EDAX and SAED patterns of the same, respectively.

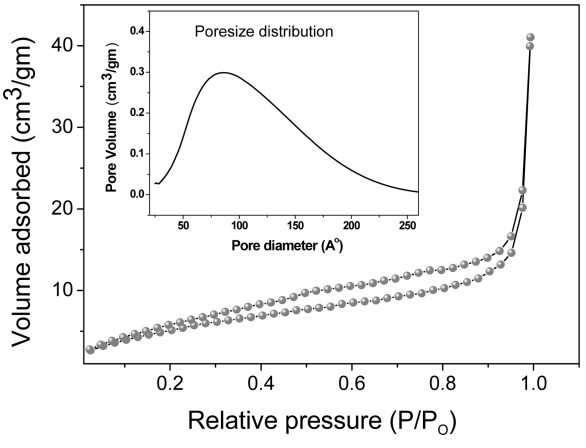

Figure 3. Nitrogen adsorption−desorption isotherm of CeO_2 nanospheres with the pore size distribution curve (inset).

pore diameter ∼90 Å and pore volume 0.57 cm^3/g. The porous CeO_2 nanospheres are obtained using a "water-in-oil"-type microemulsion-based reaction method. Generally, this type of microemulsions are prepared using two immiscible liquids and a surfactant. They are also distinguished as a thermodynamically stable system, where the aqueous phase is dispersed as droplets covered with surfactant molecules and cosurfactant molecules exist in the nonpolar organic solvent. Here, the same type of microemulsions are prepared using diethyl ether, *n*-butyl alcohol, *n*-hexane, CTAB, and aqueous solution of cerium nitrate, which led to the formation of reverse micelles. Besides the type of the emulsion, the geometric parameters of the surfactant, such as length (l), volume of the hydrophobic tail (v), and cross section of the hydrophilic head (a), play an important role in determining the nature of the micelles formed. Together, they are formulated as $P = (v/al)$. If $P > 1$, reverse micelle is formed.[20] A pictorial representation is given in the Supporting Information section (Figure S4). Indeed, it is worth mentioning that the P value is reported to be always greater than 1 for CTAB. The formation of micelles strictly depends on the surfactant concentration because it controls the CMC when the micelle formations are initiated. As delineated in the experimental section, the CMC is determined by conductometric measurements, as shown in Figure S1, where increasing the amount of CTAB from 0.2 to 1.5 g, the corresponding conductivity is recorded. The associated slope in the plot clearly shows an inflection point, indicating the generation of CMC at 0.65 g of CTAB. Upon reaching the CMC, in a water-in-oil-type system, CTAB molecules assemble themselves; commonly known as micelles. In the newly formed micelle, the hydrophobic aliphatic tails of CTAB molecules are exposed on the outside (nonpolar) of the spherical micelle and the hydrophilic heads are aggregated into the core. Because of this hydrophilic core, the aqueous solution of cerium nitrate gets dissolved in the nonpolar system. Following the same way, NH_4OH, insoluble in a nonpolar system, also gets solubilized. With the formation of micelles, distinct swelled phases, called microemulsions, are established. Then, because of the diffusion inside the system, the collision of micelles takes place, resulting in the destruction of the CTAB layer around the reverse micelles. Subsequently, an exchange of contents takes place between the aqueous droplets of two existing microemulsions,

DOI: 10.1021/acsomega.8b00146
ACS Omega 2018, 3, 4433−4440

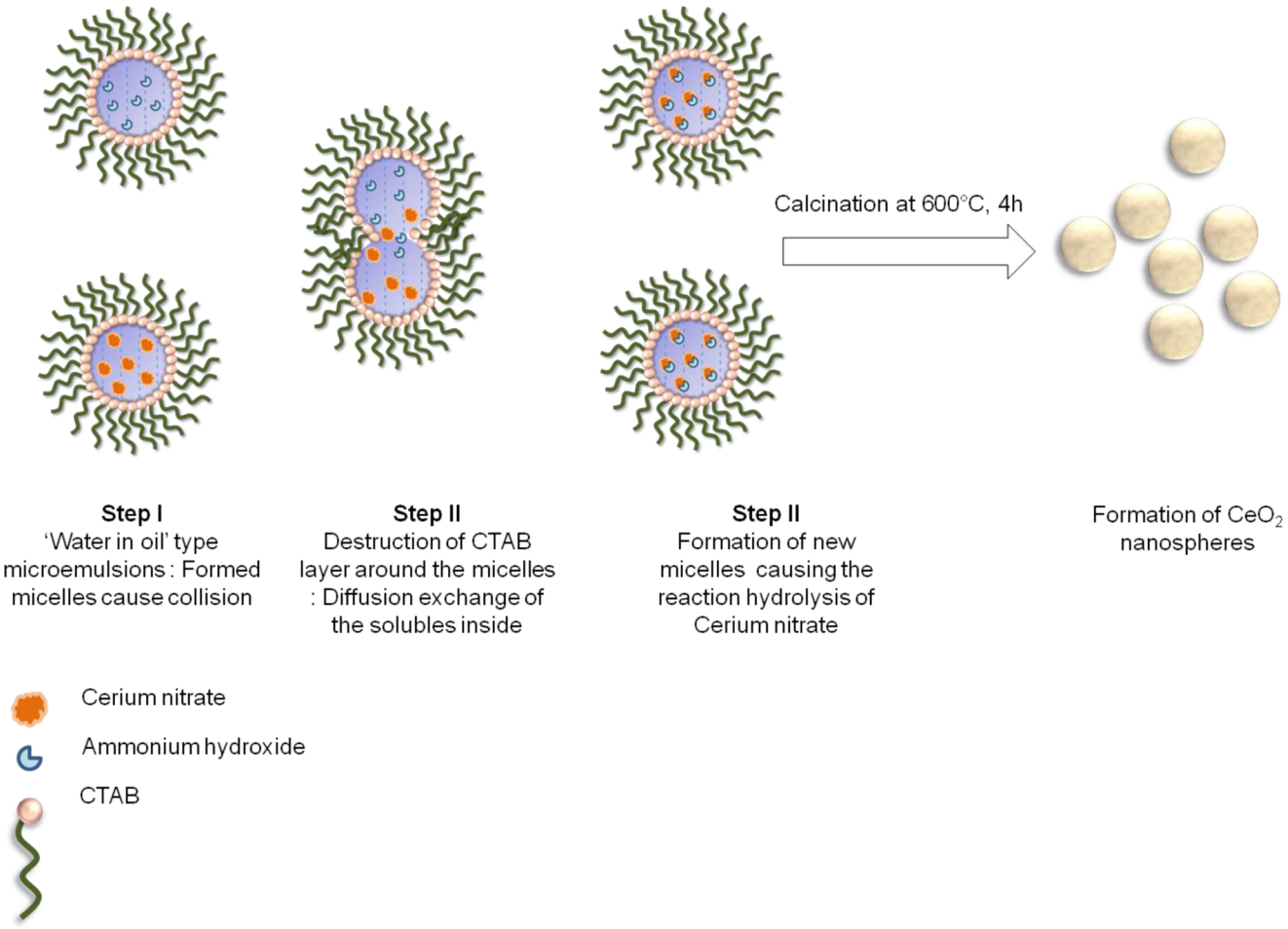

Figure 4. Plausible formation mechanism of CeO_2 nanospheres in a reverse micelle method.

which are cerium nitrate microemulsion and NH_4OH microemulsion. As a consequence, a reaction occurs between them, and this phenomenon leads to the formation of well-dispersed spherelike CeO_2 nanoparticles.[21] The corresponding schematic of the formation mechanism of CeO_2 nanospheres is illustrated in Figure 4. Here, in this work, spherical CeO_2 nanoparticles were prepared following the reverse micelle method and the concentration of the surfactant was the critical micelle concentration, constant for that particular reaction medium. Here, the cerium precursor is cerium nitrate, in which Ce is in a +3 trivalent state. Thus, one cerium nitrate molecule requires three NH_4OH molecules. Here, the concentrations of the precursors were kept in such a way that cerium nitrate is of 1 M and the 10% (w/v) NH_4OH is of ∼3 M. Thus, their molar ratio is 1:3. In the microemulsion synthesis process, the final size of the nanoparticles is restricted as the chemical reaction takes place inside the water droplets within the reversed micelles. The surfactant molecules get adsorbed on the surface of the particles to protect them from further particle growth, once the particles reach a critical size in the droplets. Thus, microemulsion methods are very useful to obtain monodispersed nanoparticles with a narrow size distribution. Here, we have varied the concentration of cerium nitrate from 0.5 to 2 M keeping the other parameters constant and the size of the resulted CeO_2 nanoparticles was analyzed using DLS measurements (Figure S5). They show a narrow size distribution and ∼50 nm as the average size of the particles in each case. However, with the increase in concentration of cerium nitrate, the formation of slightly larger particles is reported.[21] In Figure S5, the peak of the distribution is slightly shifted to the a larger particle side for the highest concentration. After several washings of the collected CeO_2 materials, some remnants of CTAB remain there. Upon calcination, the remnant surfactant gets burnt away and, simultaneously, it perforates the material, resulting in enormous porosity in CeO_2 nanospheres. The huge porosity of the material plays a pivotal role in the effective surface area and adsorption−desorption isotherm during CO gas sensing. The nature of the isotherm in Figure 3 deviates from that in the Langmuir model of adsorption. The intermediate flat portion in the isotherm is attributed to the formation of a monolayer, which is a key factor behind the better performance of the solid-state gas sensor in terms of the response (τ_{res}) and recovery (τ_{rec}) times of the said sensor. The characteristic UV−visible peak of CeO_2 is seen at 363 nm in Figure 5, and the corresponding band gap of the sensing material was obtained by plotting the Schuster−Kubelka−Munk absorption function, $(\alpha h\nu)^{1/n}$, against the photon energy ($h\nu$) according to eq 1.

$$(\alpha h\nu)^{1/n} = A(h\nu - E_g) \quad (1)$$

where A, h, n, and α are proportionality constant, Planck's constant, frequency of vibration, and absorption coefficient, respectively. Here, $n = 2$ for direct transition. The band gap is 2.88 eV, calculated from the straight line x-intercept, as presented in the inset of Figure 5. In general the band gap of

DOI: 10.1021/acsomega.8b00146
ACS Omega 2018, 3, 4433−4440

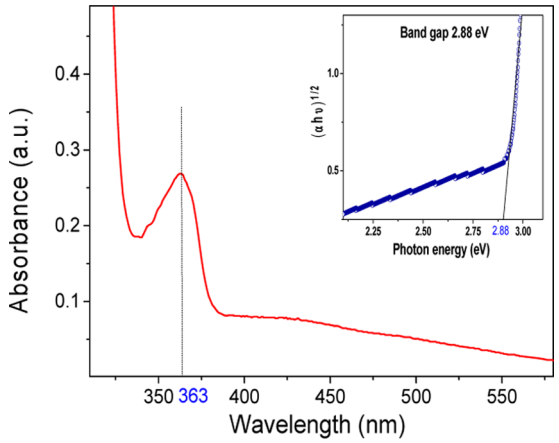

Figure 5. UV−vis spectroscopy and Schuster−Kubelka−Munk absorption function of CeO_2 nanostructures (inset), showing the corresponding band gap.

CeO_2 is ≥3 eV. Narrowing of band gap in CeO_2 nanospheres makes it a better semiconductor material for gas-sensing applications. In addition, oxygen vacancy also has a strong influence. The presence of oxygen vacancies is confirmed using PL spectroscopy (Figure S6) with excitation wavelength 320 nm. The formation of oxygen vacancies in CeO_2 is represented by the Kröger−Vink equation,[22] $O_o^{\times} + 2Ce_{Ce}^{\times} = V_o^{\bullet\bullet} + 2Ce_{Ce}' + 1/2O_2$, where $O_o^{\times}$ is the O^{2-} ion on the oxygen lattice site; $Ce_{Ce}^{\times}$ and Ce_{Ce}' are Ce^{4+} and Ce^{3+}, respectively; and $V_o^{\bullet\bullet}$ is doubly charged oxygen vacancy, and its formation releases two free electrons. These electrons are captured by Ce^{4+} and get transformed into Ce^{3+} ions. The resulted oxygen vacancies with the formation of Ce^{3+} ions lead to a lattice distortion, which has a direct correlation with the narrowing of band gap of the sensing material. As reported in the literature, the emission energy is 3.0−3.38 eV for de-excitation of the electrons to the valence band in CeO_2. The PL emission is thus assumed to be due to the transition from the 4f band of Ce to the 2p band of O, and the emission peaks ranging from 350 to 575 nm, observed in Figure S6, are assigned to the results of defects including oxygen vacancies.[23−25]

Gas-Sensing Characteristics. In our studies, carbon monoxide (at varied concentrations) was the target gas, whereas high-purity nitrogen (99.99%) was used as the diluent. During calibration, the packaged sensors were kept at the operating temperature (using an in-built heating element). Thus, when the baseline data were recorded, the sensors were exposed to laboratory air, which contains about 21% oxygen. The oxygen molecules from air get adsorbed on the surface of the metal oxide. Owing to its high electron affinity, each adsorbed oxygen atom captures free electrons in the metal oxide, forming a potential barrier at the grain boundaries of the nanoparticles. This potential barrier perturbs the electron flow, causing high sensor resistance in air (laboratory ambient). When the sensors were exposed to a reducing gas like carbon monoxide, the oxidation reaction of the target gas with adsorbed oxygen occurred at the surface of cerium oxide. Because the diluent was nitrogen gas, the partial pressure of oxygen on the sensor surface was minimized. This facilitated the oxidation reaction of carbon monoxide on the sensor surface. As a result of oxidation reaction, the surface coverage of the adsorbed oxygen on the metal oxide surface decreased and

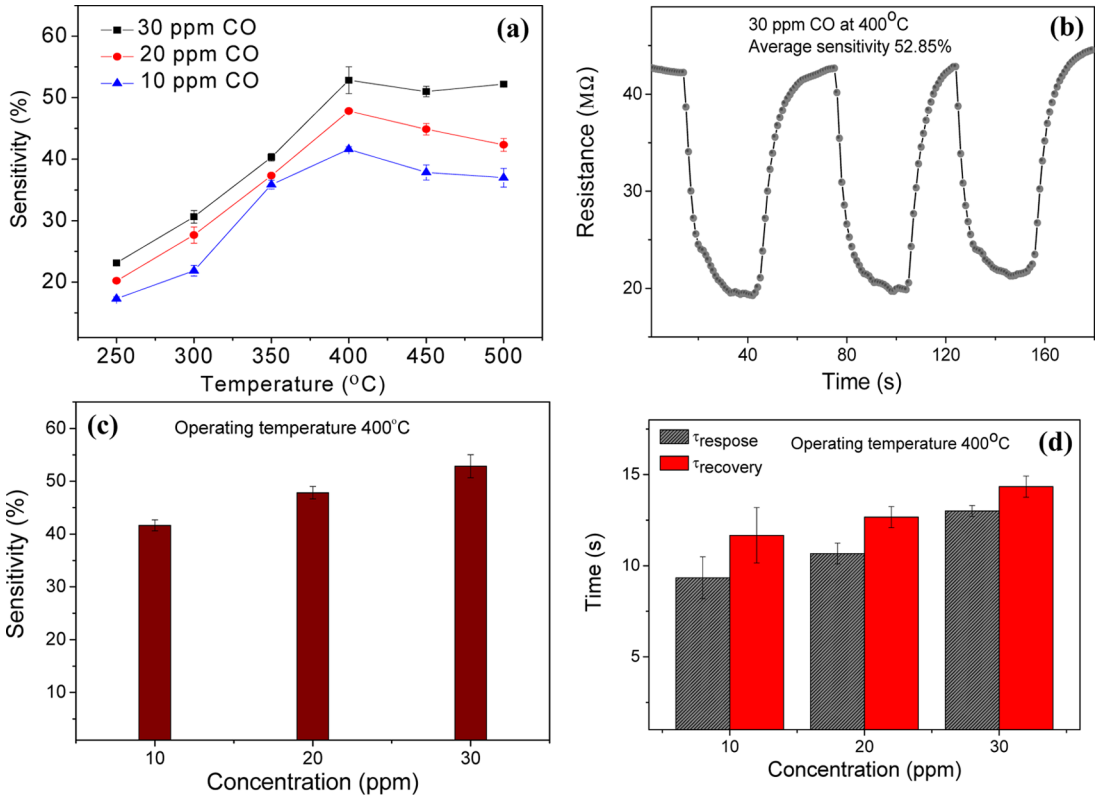

Figure 6. Sensing characteristics of CeO_2 sensors: (a) sensitivity as a function of temperature, which shows saturation after 400 °C, (b) dynamic response characteristics of 30 ppm CO at 400 °C, (c, d) sensitivity and response−recovery times as a function of concentration over the range of 10−30 ppm CO, respectively.

DOI: 10.1021/acsomega.8b00146
ACS Omega 2018, 3, 4433−4440

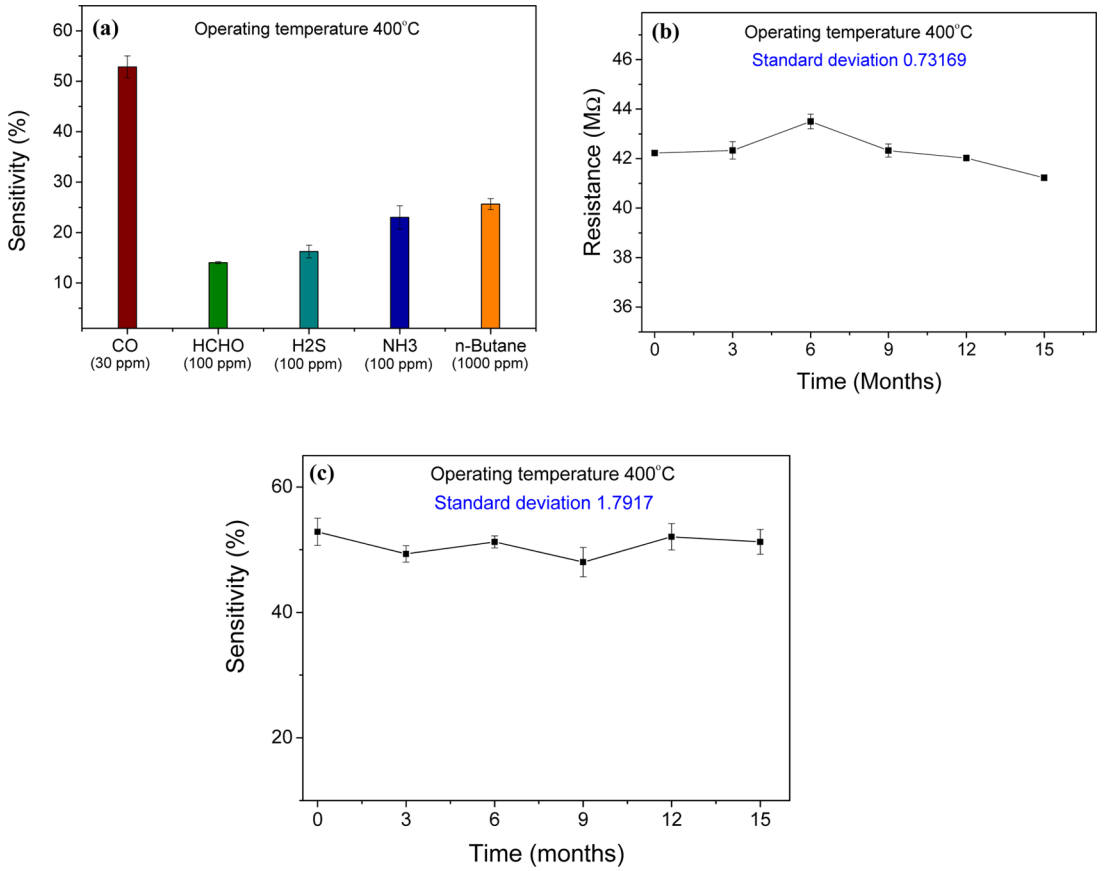

Figure 7. (a) Cross-sensitivity plot of CeO_2 sensors, (b, c) long-term stability of the sensor base resistance and long-term stability of the sensitivity under 30 ppm CO at 400 °C, respectively.

the height of the potential barrier reduced. Subsequently, the electron flow through the reduced potential barrier became facile and the sensor resistance decreased. The concentration of CO in air thus could be detected by measuring the change in resistance of the sensors. The operating temperature plays a significant role in gas-sensing measurements. To fix the operating temperature, the CeO_2 sensors were exposed to different operating temperatures ranging from 250 to 500 °C using different concentrations of CO as a target analyte. From Figure 6a, it is observed that for all of the cases, sensitivity of the sensors increases with an increase in temperature, becomes highest at 400 °C, and then attains saturation. Considering the thermal budget, 400 °C is determined as the operating temperature of the CeO_2 sensors. Figure 6b shows the representative dynamic response pattern for a pulse train of 30 ppm CO at the operating temperature. Figure 6c unfolds the sensitivity of CeO_2 sensors as a function of concentration at 400 °C, showing the increase in sensitivity as the analyte concentration increases. The corresponding dynamic response patterns are provided in Figure S7. The response time of a gas sensor to trigger an alarm and the recovery time, required for a sensor to be ready for the next target analyte, are of paramount importance for real-time application purposes in the sensor field. Conventionally, the response time (τ_{res}) is defined as the time required by the sensor to reach 90% of its saturation resistance value after being exposed to the target analyte and the recovery time (τ_{rec}) is the time lag to attain its 90% baseline value after the target analyte is withdrawn. Deploying the CeO_2 sensors under different concentrations of CO ranging from 10 to 30 ppm, the results exhibit excellent response and recovery times of the sensors. The response times (τ_{res}) of the sensors are 9, 10, and 13 s under 10, 20, and 30 ppm CO, respectively, and the recovery times (τ_{rec}) are 11, 12, and 14, respectively, under the same series of concentrations (Figure 6d). The cross-sensitivity of the sensors was checked against the most common interfering gases with higher concentrations. Figure 7a reveals that 10-fold higher concentrations of formaldehyde, hydrogen sulfide, and ammonia and 100 times higher concentration of a hydrocarbon (*n*-butane) resulted in much lower sensitivity compared to that of 30 ppm CO in air. In this article, the base resistance of the sensors and their sensitivity toward CO were monitored for a span of 15 months (Figure 7b,c respectively). During the entire tenure of 15 months, the sensors show good stability of base resistance with a standard deviation of less than 1 (Figure 7b) and an almost constant sensitivity was observed with a standard deviation of less than 2 (Figure 7c). The high effective surface area of CeO_2 nanospheres provides enhanced surface coverage of oxygen adsorbates, and the surface catalytic properties of the CeO_2 material promote the oxidation of CO. The abundant oxygen vacancies of CeO_2, high oxygen storage capacity, and facile transition between its Ce^{3+} and Ce^{4+} oxidation states result in enhanced sensitivity during CO sensing. According to the basic n-type solid-state gas-sensing theory, oxygen molecules of air dissociatively or non-dissociatively adsorb on the metal oxide surface in a random manner, resulting in trapping of electrons from the conduction band and formation of charged oxygen molecular species like O_{ads}^{2-}, O_{ads}^{-}, and O_{ads}^{2-}. These adatoms are electrostatically stabilized near the cations at the surface of the metal oxide. CO, which is reducing in nature, reacts with these charged oxygen

DOI: 10.1021/acsomega.8b00146
ACS Omega 2018, 3, 4433−4440

species and, as a consequence, the trapped electrons are again free to the conduction band, resulting in a drop in resistance. Reportedly, this occurs in the temperature range of 100−500 °C, which is usually the operating temperature of the sensors of this genre. Initially, physisorption of CO takes place via dipole bonding to the metal-oxide−semiconductor surface, removing the electrons from high oxygen vacancy, and a charge transfer mechanism subsequently results in the formation of a chemical bond with the semiconductor surface atoms, commonly known as chemisorption. The facile monolayer adsorption of CO molecules (may be assigned from adsorption isotherm, Figure 3) on the surface of a surface-active CeO_2 sensor plays a pivotal role in the staggering response time, 9 s.

During the physical adsorption, target gas molecules are attracted to the sensor surface to form adsorption layers, and then, depending on gas concentration, they may be multilayer or monolayer in nature. The BET adsorption−desorption isotherm and the pore size distribution (Figure 3) of the CeO_2 sensing material lead to the high probability of formation of monolayers across the sensor surface. The active sites of CeO_2 escalate the response time. Additionally, the formation of monolayer propagates the conductive charge transfer across the material, promoting the same. The monolayer formation also favors the process of desorption, resulting in a faster recovery time of the sensors (Figure 6d). The above observations suggest that the undoped CeO_2 nanospheres with high surface area are a good choice as a material for CO sensors showing fast response and recovery features and appreciable stability over a long period of time.

CONCLUSIONS

Highly porous well-dispersed CeO_2 nanospheres were synthesized via the reverse micelle precipitation method. The undoped pristine material was deployed for low-concentration (30−10 ppm) CO gas sensing at an optimum operating temperature, and the sensors, comprising the same, showed appreciable sensitivity with rapid response and recovery times with significant selectivity as well. The LOD of the ready-to-use sensors is down to 10 ppm with commendable sensitivity of ∼43% and that too has the response time of less than 10 s. The sensor parameters of the materials are well corroborated to the morphology, high surface area, and porosity of the material. Compared with previously reported studies, this article enlightens the potential of undoped pristine CeO_2 nanomaterials in the development of a CO gas sensor, opening a new direction toward the usage of bare CeO_2 in the gas-sensing filed.

ASSOCIATED CONTENT

Supporting Information

The Supporting Information is available free of charge on the ACS Publications website at DOI: 10.1021/acsomega.8b00146.

Conductivity measurements to determine CMC, FESEM image of CeO_2 nanospheers, FESEM micrograph of calcined CeO_2 nanospheres HRTEM (inset), pictorial representation of the surfactant behind the micellar formation, DLS measurements of CeO_2 synthesized using different concentrations of cerium precursor, photoluminescence spectroscopy, and dynamic response characteristics of the sensor for 20 and 10 ppm carbon monoxide gas (PDF)

AUTHOR INFORMATION

Corresponding Author

*E-mail: sroy@cgcri.res.in. Tel: +91 33 23223427.

ORCID

Somenath Roy: 0000-0002-3352-0534

Notes

The authors declare no competing financial interest.

ACKNOWLEDGMENTS

The research work was partially supported by the Council of Scientific and Industrial Research (CSIR), Government of India, through its 12th five year plan network project "MULTIFUN" (Grant number: CSC-0101) and DST Nano-mission, Government of India (Grant number: SR/NM/NT-1001/2015(C)). D.M. is grateful to the Department of Science and Technology (DST), Government of India, for providing the INSPIRE fellowship. The laboratory facilities of DST-CSIR Sensor Hub, Kolkata, and S.N. Bose National Centre for Basic Sciences, Kolkata, have been used for this work.

REFERENCES

(1) Da Silva, J. L. F.; Ganduglia-Pirovano, M. V.; Sauer, J.; Bayer, V.; Kresse, G. Hybrid functionals applied to rare-earth oxides: The example of ceria. *Phys. Rev. B.* **2007**, *75*, No. 045121.

(2) Tibiletti, D.; Amieiro- Fonseca, A.; Burch, R.; Chen, Y.; Fisher, J. M.; Goguet, A.; Hardacre, C.; Hu, P.; Thompsett, D. DFT and In Situ EXAFS Investigation of Gold/Ceria−Zirconia Low-Temperature Water Gas Shift Catalysts: Identification of the Nature of the Active Form of Gold. *J. Phys. Chem. B* **2005**, *109*, 22553−22559.

(3) Harrison, P. G.; Ball, I. K.; Azelee, W.; Daniel, W.; Goldfar, D. Nature and Surface Redox Properties of Copper(II)-Promoted Cerium (IV) Oxide CO-Oxidation Catalysts. *Chem. Mater.* **2000**, *12*, 3715−3725.

(4) Trovarelli, A. *Catalysis by Ceria and Related Materials*; Imperial College Press: London, 2002.

(5) Liu, Y.; Ding, Y.; Zhang, L.; Gao, P. X.; Lei, Y. CeO_2 nanofibers for in situ O_2 and CO sensing in harsh environments. *RSC Adv.* **2012**, *2*, 5193−5198.

(6) Izu, N.; Shin, W.; Murayama, N.; Kanzaki, S. Resistive oxygen gas sensors based on CeO_2 fine powder prepared using mist pyrolysis. *Sens. Actuators, B* **2002**, *87*, 95−98.

(7) http://www.euro.who.int/__data/assets/pdf_file/0005/74732/E71922.pdf.

(8) https://www.osha.gov/dts/sltc/methods/inorganic/id209/id209.htm.

(9) Beie, H. J.; Gnörich, A. Oxygen gas sensors based on CeO_2 thick and thin films. *Sens. Actuators, B* **1991**, *4*, 393−399.

(10) Jasinski, P.; Suzuki, T.; Anderson, H. U. Nanocrystalline undoped ceria oxygen sensor. *Sens. Actuators, B* **2003**, *95*, 73−77.

(11) Lee, J. H. Gas sensors using hierarchical and hollow oxide nanostructures: Overview. *Sens. Actuators, B* **2009**, *140*, 319−336.

(12) Yoo, J.; Yoon, H.; Wachsman, E. D. Sensing propeties of MO_x/YSZ/Pt (MO_x = Cr_2O_3,SnO_2, CeO_2) potentometric sensor for NO_2 detection. *J. Electrochem. Soc.* **2006**, *153*, H217−H221.

(13) Barreca, D.; Gasparotto, A.; Maccato, C.; Maragno, C.; Tondello, E.; Comini, E.; Sberveglieri, G. Columnar CeO_2 nanostructures for sensor application. *Nanotechnology* **2007**, *18*, No. 125502.

(14) Xuan, Y.; Hu, J.; Xu, K.; Hou, X.; Lv, Y. Development of sensitive carbon disulfide sensor by using its cataluminescence on nanosized-CeO_2. *Sens. Actuators, B* **2009**, *136*, 218−223.

(15) Izu, N.; Shin, W.; Matsubara, I.; Murayama, N. Inflence of SO_2 gas on output of resistive oxygen sensors using CeO_2 and $Ce_{0.8}Zr_{0.2}O_2$. *J. Electrochem. Soc.* **2005**, *152*, H111−H114.

DOI: 10.1021/acsomega.8b00146
ACS Omega 2018, 3, 4433−4440

(16) Izu, N.; Itoh, T.; Shin, W.; Matsubara, I.; Murayama, N. CO sensor having two Zr-doped CeO_2 films with and without catalyst layer. *Electrochem. Solid-State Lett.* **2007**, *10*, J37−J40.
(17) Majumder, D.; Datta, A.; Mitra, M. K.; Roy, S. Kinetic analysis of low concentration CO detection by Au-loaded cerium oxide sensors. *RSC Adv.* **2016**, *6*, 92989−92995.
(18) Durrani, S. M. A.; Al-Kuhaili, M. F.; Bakhtiari, I. A. Carbon monoxide gas-sensing properties of electronbeam deposited cerium oxide thin films. *Sens. Actuators, B* **2008**, *134*, 934−939.
(19) Michel, C. R.; Martínez-Preciadob, H. A. CO sensor based on thick films of 3D hierarchical CeO_2 architectures. *Sens. Actuators, B* **2014**, *197*, 177−184.
(20) Pileni, M. P. Reverse micelles as microreactors. *J. Phys. Chem.* **1993**, *97*, 6961−6973.
(21) Masui, T.; Fujiwara, K.; Machida, K.; Adachi, G.; et al. Characterization of Cerium (IV) Oxide Ultrafine Particles Prepared Using Reversed Micelles. *Chem. Mater.* **1997**, *9*, 2197−2204.
(22) Shoko, E.; Smith, M. F.; McKenzie, R. H. Charge distribution near bulk oxygen vacancies in cerium oxides. *J. Phys.: Condens. Matter* **2010**, *22*, No. 223201.
(23) Corma, A.; Atienza, P.; Garcia, H.; Chane-Ching, J. Y. Hierarchically mesostructured doped CeO2 with potential for solar-cell use. *Nat. Mater.* **2004**, *3*, 394−397.
(24) Yu, S. H.; Colfen, H.; Fischer, A. High quality CeO_2 nanocrystals stabilized by a double hydrophilic block copolymer. *Colloids Surf., A* **2004**, *243*, 49−52.
(25) Morshed, A. H.; Moussa, M. E.; Bedair, S. M.; Leonard, R.; Liu, S. X.; Masry, N. E. Violet/blue emission from epitaxial cerium oxide films on silicon substrates. *Appl. Phys. Lett.* **1997**, *70*, 1647.

DOI: 10.1021/acsomega.8b00146
ACS Omega 2018, 3, 4433−4440